MoJin Zhou, YeHua Jiang* and XiaoYu Chong*

Interface transition layer interaction mechanism for ZTA_p/HCCI composites

DOI 10.1515/secm-2016-0332
Received November 6, 2016; accepted June 2, 2017; previously published online July 26, 2017

Abstract: ZrO_2-toughened Al_2O_3 (ZTA, 40%) ceramic particles reinforced by high chromium cast iron (HCCI) matrix composites were fabricated by casting infiltration. The interaction between the ZTA ceramic particles and the matrix by the interface transition layer (ITL) was investigated. From the perspective of interfacial bonding, the ceramic particles and HCCI experienced metallurgical bonding by the ITL. Electron probe microanalysis results demonstrated that Cr, Fe, and Mn diffused from the matrix to the ITL. Transmission electron microscopy revealed that the main phases in the transition layer were glassy. The wear resistance of the composites with the transition layer was better than those without, as indicated by the three-body abrasive wear tester.

Keywords: composites; glass-ceramic phase; interface transition layer; ZTA.

1 Introduction

Currently, traditional wear resistance materials (i.e. white cast iron, high manganese steel, alloy steel) are insufficient to meet the demands of modern industry. The structure of material composites has become a new research direction encompassing ceramic/metal matrix wear resistance composites [1, 2]. The ceramic particle reinforced metal matrix composites (CPRMMCs) involve the addition of ceramic particles to the molten metal often obtained by spontaneous reaction during liquid metal solidification [3–6]. The CPRMMC materials not only exhibit high hardness and high modulus of the ceramic particles but also good toughness of the metal. However, the critical issue is how to solve the problem of the conjunction between the metal matrix and the ceramic particles. The ceramic-metal composites material of Al_2O_3/Fe was obtained by casting metal infiltration [7]. It reacts with alumina and generates a thin $FeAl_2O_4$ spinel layer when the molten iron infiltrates the gap between alumina particles. Tungsten carbide (WC) particles due to their high hardness can also be used as reinforcement to reinforced iron or steel matrix that is usually obtained by sintering or vacuum evaporative pattern casting and obtain the phase of Fe_3W_3C. However, WC cannot be widely applied due to its high price. WC has good wettability for iron and can generate Fe_3W_3C with iron under certain conditions, but the wetting contact angle between Al_2O_3 and iron is as high as 140°. The hardness of the WC particles is 2093HV30 – higher than that of Al_2O_3 particles (1700HV30) [8–12]. Ru et al. obtained alumina particles by nickel plating reinforced iron matrix composites, where the wear resistance of the alumina particles is higher than that of the matrix [13]. In this manner, interfacial-bonding improvement mainly relies on the reaction between the reinforcements and the metal matrix. However, it also affects the performance of the reinforcements. Usually, to improve the surface wettability of ceramic particles, they are often plated with a metal element. The combination is essentially a mechanical binding mode [14, 15].

In ZTA ceramic particles, zirconia is present in a metastable tetragonal phase. When the material is cooled to room temperature after sintering, the partial grain size increases above the critical particle size of ZrO_2 when t-m phase transition occurs. The volume of the ZTA particles will expand such that microcracks are generated in the matrix, and the expansion of the main crack acts as a bifurcation or passivation to improve the fracture toughness of the particle. It will form a certain residual stress in the matrix after ZrO_2 undergoes phase transformation. When the matrix is subjected to residual stress, the internal stress and external stress will cancel each other and the strength of the material will improve [16, 17]. Pure alumina is very brittle that a crack would be generated when phase change occurs. ZrO_2-toughened Al_2O_3 (ZTA) ceramic particles combine high strength and high hardness that can improve the wear resistance of the composites, which

***Corresponding authors: YeHua Jiang,** Faculty of Material Science and Engineering, Kunming University of Science and Technology, Kunming 650093, People's Republic of China,
Phone/fax: +86 871 65136755, e-mail: jiangyehua@kmust.edu.cn; and **XiaoYu Chong,** Faculty of Material Science and Engineering, Kunming University of Science and Technology, Kunming 650093, People's Republic of China; and Department of Materials Science and Engineering, Pennsylvania State University, University Park, PA 16802, USA, e-mail: 617458806@qq.com
MoJin Zhou: Faculty of Material Science and Engineering, Kunming University of Science and Technology, Kunming 650093, People's Republic of China

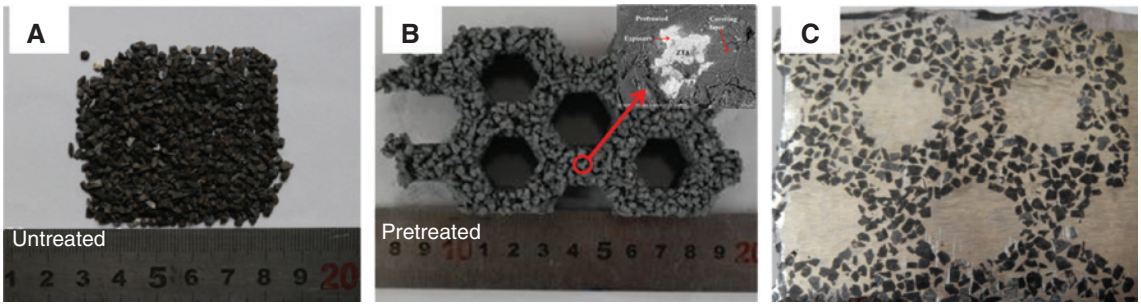

Figure 1: Macrographs of composite: (A) ceramic particles; (B) porous network of the preform; (C) CPRMMC.

makes ZTA suitable for reinforcement. In this paper, ZTA (40%) particles are used as reinforcements. Their toughness and thermal shock resistance are better than those of pure alumina ceramic particles [12, 16]. The ZTA particles should be pretreated when used, whereby the surface of the particles is covered with ceramic powder. The molten high chromium cast iron (HCCI) infiltrates the gap between the ZTA particles by gravity casting. It reacts with the powder and generates an interface transition layer (ITL) of glass phases at the interface. The ITL can improve the interfacial bonding properties. The wear resistance of the composites is also investigated using a three-body abrasive wear test.

2 Materials and methods

2.1 Preparation for the composites

Irregular ceramic particles are shown in Figure 1A. The size of the particles is 12–14 ASTM mesh. The chemical composition is displayed in Table 1. The physical and mechanical properties are shown in Table 2. Usually, the alumina particles are white; however, the ZTA ceramic is black in this paper. This is related to the preparation process of the ZTA ceramic particles. The preparation process is usually by melting, calcination, and crushing, finally obtaining the desired size of particles. It is also related to the toughened phase of ZrO_2. The ZTA particles reinforced with HCCI matrix composites are synthesized by gravity casting (Figure 1C) and their honeycomb structure is shown in Figure 1B.

Conventional composites are shown in Figure 2. The direction of metal infiltration is only one, which limits the material composite layer thickness. The composites of the honeycomb structure are conducive to molten metal infiltration. It is beneficial to improve the composite efficiency of metal and ceramic particles [18].

The density of the ZTA particles is ρz; the weight of the ceramic particles is mass Mz; and their volume is V'. Through the formula $Vz = Mz/\rho z$, the corresponding volume Vz is obtained. The porosity of the preform is calculated as follows:

$$w = \frac{V_Z - V'}{V_Z} \times 100\%.$$

The porosity of ZTA is 52%.

The composites of ZTA particle reinforced HCCI are synthesized by gravity casting. The specific processes

Table 1: Chemical composition of the ceramic particles.

Composition	Al_2O_3	ZrO_2	TiO_2	Fe_2O_3	Others
Mass fraction (wt.%)	55	40.0	3.0	0.7	1.3

Table 2: Physical and mechanical properties of the ceramic particles.

Material	Melting point (°C)	Hardness (kN/mm²)	Density (g/cm³)	Breaking strength (N)
ZTA (40% ZrO_2)	1800	19	4.63	97

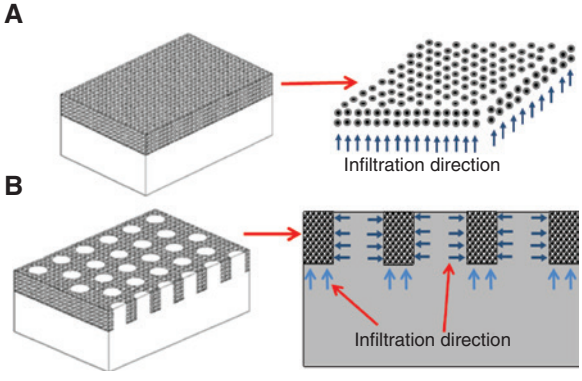

Figure 2: Infiltration casting schematic: (A) layered composites; (B) honeycomb structure composites [8].

are described as follows: (i) First, raw materials are weighed by mass ratio and then ball-milled for about 6 h with ethanol. The chemical composition and proportion of raw materials are shown in Table 3. (ii) Then, the ceramic powder (about 4 wt.% of the ceramic particles) and water glass are mixed by mass fractions in 1:1 proportion (Figure 3). Thereafter, the particles are sufficiently stirred to obtain homogeneous samples and filled into a mold. The molds are placed in a box furnace and heated at 473 K for 2 h. (iii) Third, the preforms are placed into a sand mold cavity and poured into molten HCCI. The chemical compositions of the HCCI are displayed in Table 4. The furnace used was a medium frequency induction; the weight was 150 kg and the pouring temperature was about 1723–1823 K.

Table 3: Composition and proportion of ceramic powders.

Ceramic powders	α-Al_2O_3	TiO_2	ZrO_2	CaO	B_4C
Mass fraction (wt.%)	32	4	8	12	4
Size (μm)	3.8	0.4	0.4	3	3

2.2 Three-body abrasive wear test

The three-body abrasive wear behavior of the composites was investigated using a MMH-5 block-on-ring tester (Figure 4A). The abrasives used were loose quartz sands (SiO_2, HV900–1300, 25–40 ASTM mesh). The rotating speed of the main axle was 50 rpm/min and the test force of the single axle was 50 N. Each sample was tested for 5 h and the time of each grinding process was 1 h. After each process, the samples were placed into a beaker containing alcohol in an ultrasonic cleaner, and the mass loss was measured by using an electronic balance with an accuracy of 0.0001 g. Figure 3B shows that the size of the wear sample was 25 mm × 25 mm × 15 mm.

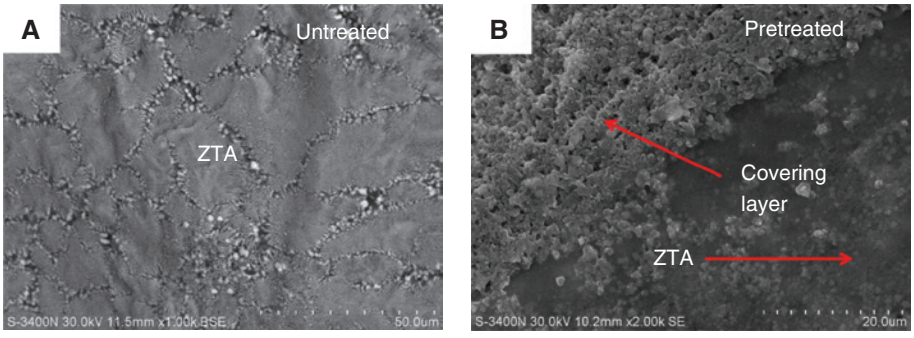

Figure 3: ZTA particles: (A) untreated; (B) pretreated.

Table 4: Chemical composition of HCCI.

Element	C	Cr	Mn	Si	Ni	Mo
Mass fraction (wt.%)	2.8–3.2	25–28	0.8–1.2	0.5–0.6	0.3–0.5	0.3–0.5

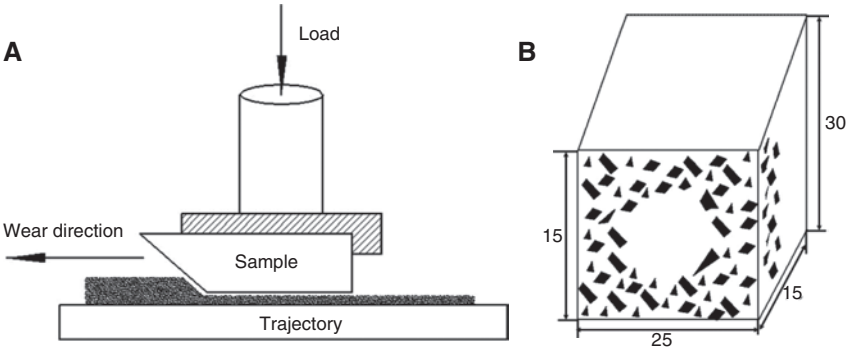

Figure 4: Schematic diagram of three-body abrasive wear test: (A) diagram of wear principle; (B) size of wear samples.

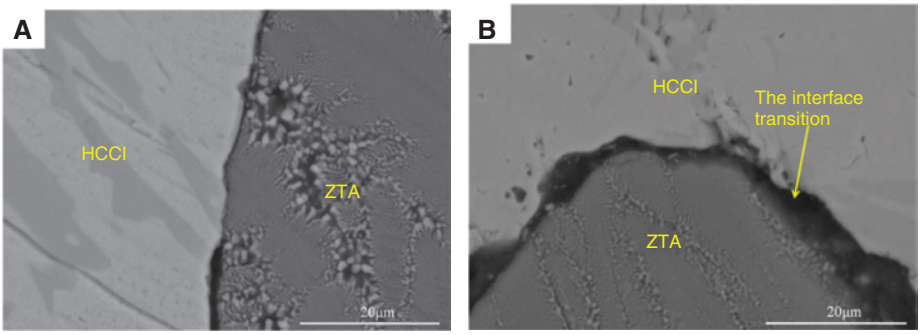

Figure 5: SEM images of the composite interface: (A) S_N; (B) S_Y.

The wear resistance of the material can be measured by mass loss, volume loss, relative wear resistance, and wear resistance rate. The composite area varies with the HCCI and ceramic particles. Under the same conditions of mass loss, the amount of volume loss was different. In this paper, the amount of volume loss was used. The volume loss of the material was calculated as follows.

The average density ρ of the composites was calculated as

$$\rho = f \cdot \rho_1 + (1-f) \cdot \rho_2, \quad (1)$$

where ρ_1 and ρ_2 represent the density of the particles and metal matrix, respectively; m_1 and m_2 represent the quality of the composites before and after abrasive wear, respectively; and f_1 represents the particles-occupied volume fraction of the composites. The volume loss of the wear samples can be calculated using the following formula:

$$V = (m_1 - m_2)/\rho. \quad (2)$$

The density of the HCCI was 7.8 g/cm^3 and the composite area was 6.22 g/cm^3.

3 Results and discussion

3.1 Structure of interface

Figure 5A and B (S-3400N; Hitachi, Japan) show the composite samples without and with ceramic powder, respectively. From Figure 5A, it can be seen that there is no ITL in the interface, only a "gully". Ceramic particles joined with a metal matrix depend on the wetting action and form a mechanical combination. From Figure 5B, it can be seen that there is a transition layer at the interface, which has better abrasion resistance under the same condition.

Figure 6 shows the X-ray diffraction pattern (D/max2200; Rigaku, Japan), which is the result of the reaction of the metal with the particles. This result can be calculated from the B_4C reaction with the metal matrix.

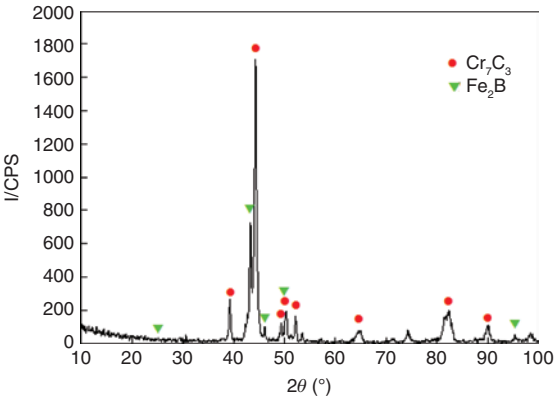

Figure 6: X-ray diffraction pattern of the metal between ceramic particles.

From the composite interface plane energy spectrum (Figure 7), it can be seen that the main elements at the interface were Na, Al, Si, and Fe. The Fe element diffused into the ITL that led to the HCCI and the ITL bonding strongly together.

The ITL was examined by electron probe microanalysis (EPMA; EPMA-1600; Shimadzu, Japan). In Figure 8, different colors represent different phases and the same colors represent the same phases. The energy spectral results of EPMA are shown in Table 5. From the table, it was calculated that the elements in the ITL were the Al_2O_3-SiO_2-CaO-Na_2O system. The presence of Cr, Fe, and Mn indicates that the elements in the matrix also diffused into the ITL. Figure 8 shows that the particles had the same colors as the transition layer. This indicates that the phases of the particles were similar to the phases in the transition layer, and that these phases merged together. For the same reason, the HCCI and the transition layer completed metallurgical bonding by diffusion and reaction. If the particles are combined with HCCI in the transition layer, the problem of the composite's interface

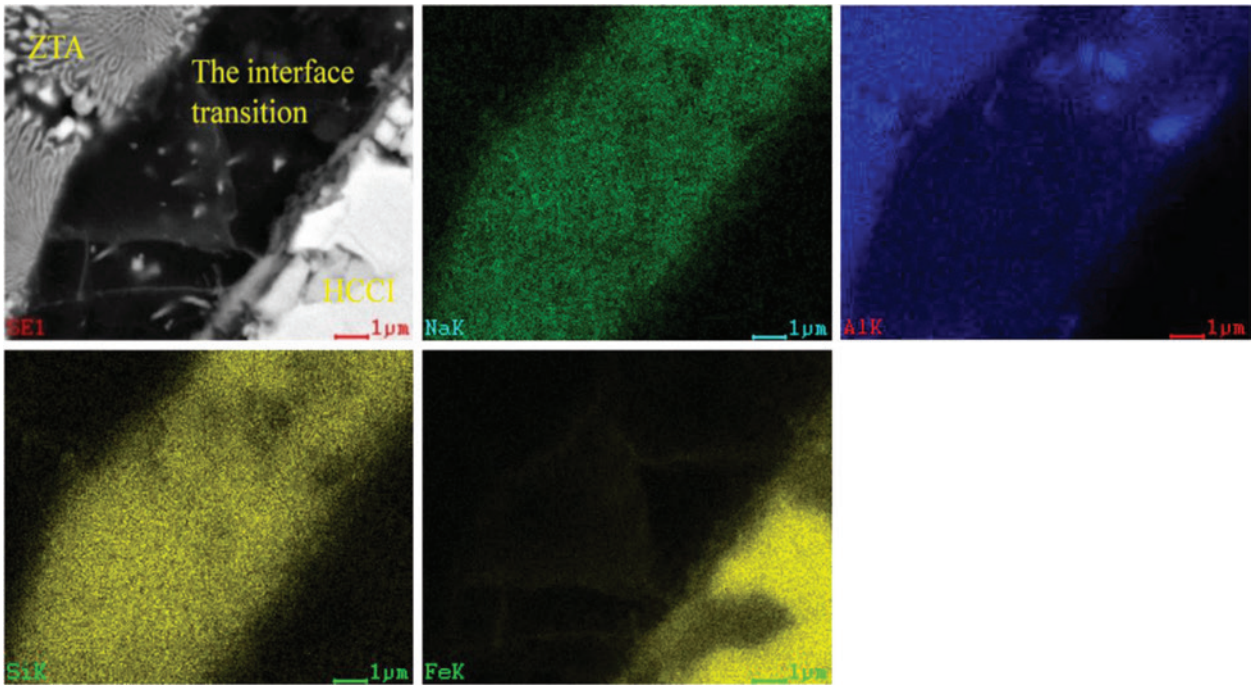

Figure 7: Interface plane energy spectrum of the composite.

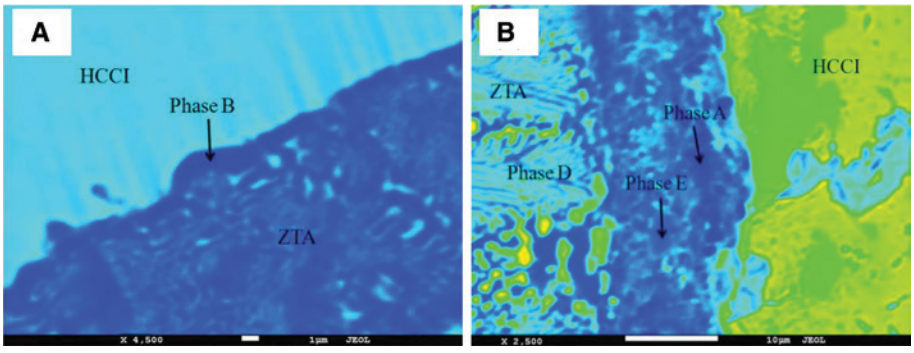

Figure 8: Interfacial transition layer by EPMA.

Table 5: Energy spectrum of EPMA.

Phases (norm%)	Na_2O	Al_2O_3	FeO	CaO	TiO_2	SiO_2	Cr_2O_3	MnO	ZrO_2
A	1.869	16.836	29.977	2.24	0.454	4.852	41.212	1.617	0.943
B	0.027	54.548		0.039	3.516	0.713	1.835	0.376	38.947
E	9.653	42.193		0.636	0.487	34.401	11.712	0.839	0.08
D	0.031	59.556		0.025	2.721	0.105	0.916	0.123	37.241

bonding between the ceramic particles and the matrix can be solved.

Transmission electron microscope (TEM) images of the ITL were obtained using a FEI Helios Nanolab 600i and FEI TECNAI G2 F20 S-TWIN. We obtained the TEM specimen of ITL by focused ion beam. These are shown in Figure 9. As can be seen from the figure, the ZTA particles and the ITL at the junction did not form a clear interface. Combined with the results of the electron probe microanalysis, it can be concluded that the particles and the ITL were combined together by interdiffusion between the particles and the ITL. At the same time, the main

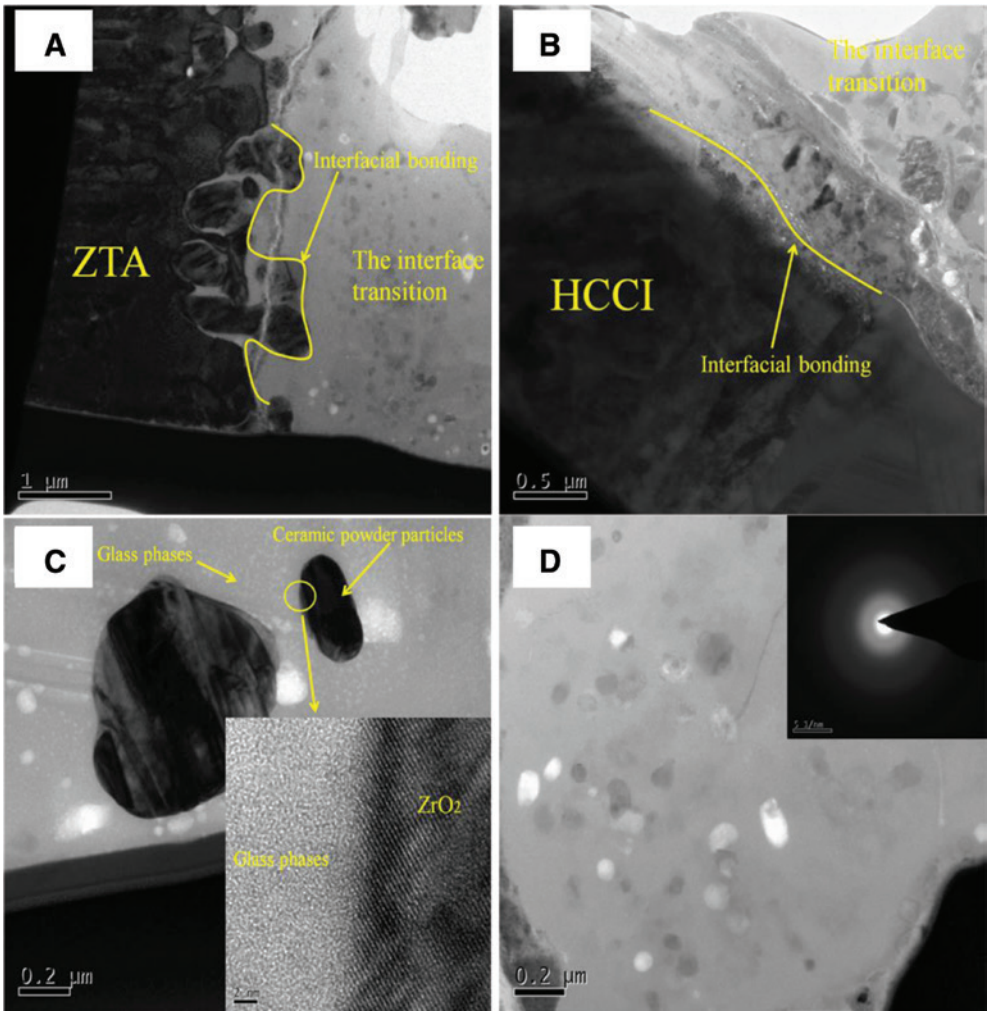

Figure 9: TEM images of the ITL: (A) ZTA combined with the ITL; (B) HCCI combined with the ITL; (C and D) ITL.

components of the particles were alumina and zirconia. The same components were present in the transition layer, which promoted wetting between the transition layer and the particles (Figure 9A). The same occurred between the HCCI and the interface transition, which were combined by diffusion (Figure 9B). By analyzing the ITL, it can be seen that the phases were amorphous and micro undissolved ceramic powder particles (Figure 9C,D). The phases in the interface transition were glass-ceramic.

The presence of ceramic powders in the preform can improve the interface bonding of the ZTA particles and the HCCI. The main composition of the binder is Na_2O and SiO_2; the main interface reaction system is Al_2O_3-SiO_2-CaO-Na_2O. The glass-ceramic phases are obtained under high-temperature conditions [19–23]. The molten metal that contacts the particles induces a rapid cooling effect, as the coefficient of thermal expansion between the metal and the particles is different. It will generate thermal stress at the interface of the composites due to the effects of thermal expansion and contraction [24]. The glass-ceramic phases have a good fluidity at high temperature and can absorb the thermal stress and obtain a good combination of ceramic particles and the metal matrix [18, 25]. The ceramic powders can react with Fe as follows [26–28]:

$$5Fe + B_4C = Fe_2B + 3FeB + C. \quad (3)$$

$$FeO + TiO_2 = FeO \cdot TiO_2. \quad (4)$$

$$FeO + Na_2O \cdot SiO_2 = FeO \cdot SiO_2 + Na_2O. \quad (5)$$

The chemical reaction is investigated by thermodynamic calculations, which are dependent on the Gibbs free energy. The reaction ΔG_m is given by the Gibbs-Helmholtz equation:

$$\Delta G_m = \Delta H_m - T\Delta S_m. \quad (6)$$

Here, the conventional standard enthalpies of the phases are calculated using the following relationship:

$$\Delta H_m = \Delta H_{298} + \int_{298}^{T_{tr}} C_{p_1}\,\mathrm{d}T + n\Delta H_{tr} + \int_{T_{tr}}^{T} C_{p_2}\,\mathrm{d}T. \quad (7)$$

Here, C_{P1} and C_{P2} represent different phase molar heat capacities at constant pressure; T_{tr} represents the transformation point; and ΔH_{tr} represents the heat of the phase transition. Figure 10 shows the relationship between the temperature and the reaction enthalpy or Gibbs free energy. According to the basic principles of thermodynamics, a reaction will be spontaneous only if the change in Gibbs free energy (ΔG_m) is negative. Figure 10B shows that the chemical reactions [Eqs. (3)–(5)] can carry on.

3.2 Mechanical properties of the transition layer

A nano-indentation test was implemented using a nano-indentation instrument (TI950; Hysitron, USA). Figure 11 is a representative load-displacement (F-h) curve, which was analyzed based on the Oliver and Pharr method. Each point had the same peak load of 10,000 mN and the loading and unloading rates were both maintained at 1 mN/s (Figure 11C). During indenting, forces and displacement were recorded to generate load-depth curves (Figure 11A). The Oliver and Pharr method was applied to calculate the hardness (H) and Young's modulus (E), as shown in the following relations:

$$H = \frac{F_{\max}}{A}, \quad (8)$$

$$E_r = \frac{1-\nu^2}{E} + \frac{1-\nu_i^2}{E_i}, \quad (9)$$

$$S = \frac{\mathrm{d}p}{\mathrm{d}h} = \frac{2}{\sqrt{\pi}} E_r \sqrt{A}, \quad (10)$$

where $F_{\max}$ is the maximum applied load; A is the projected contact area between the indenter tip and the specimen

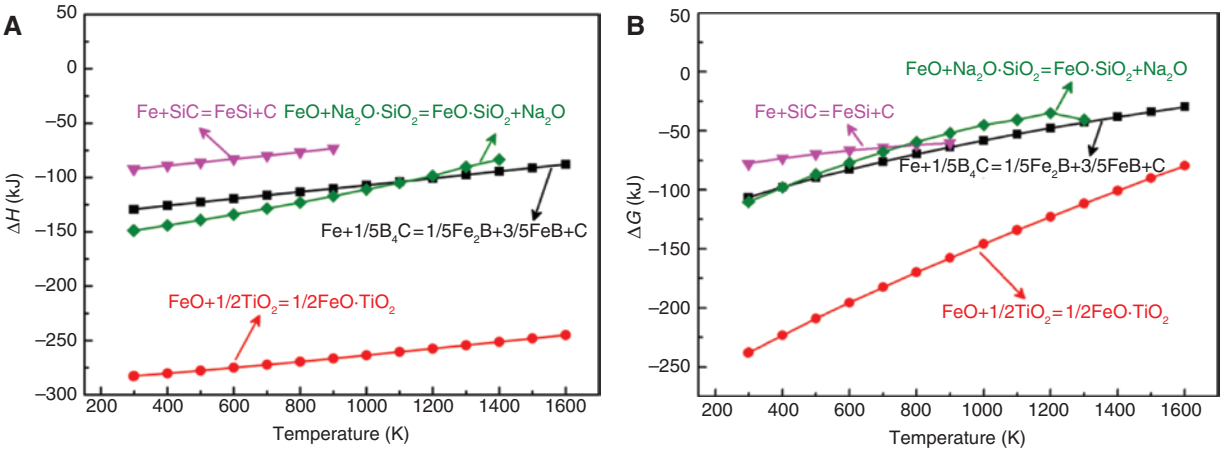

Figure 10: Relationship between temperature and reaction enthalpy or Gibbs free energy: (A) temperature and reaction enthalpy; (B) temperature and Gibbs free energy.

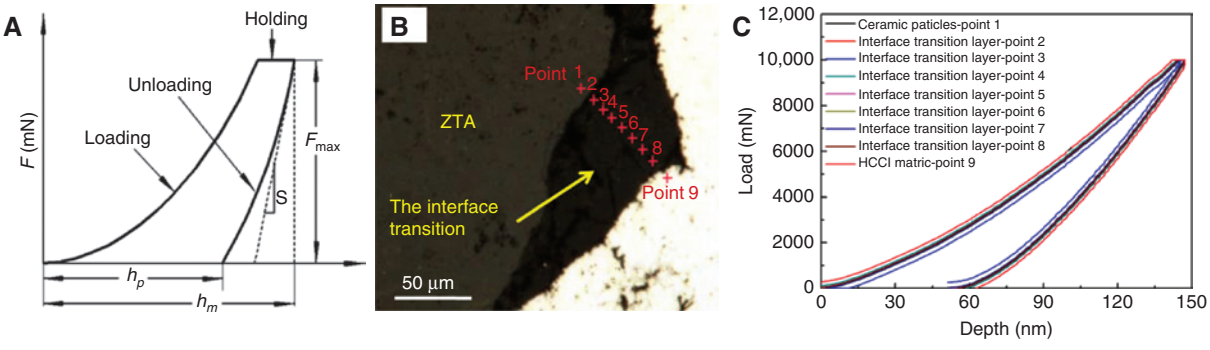

Figure 11: Representative load-displacement (F-h) curve analysis based on the Oliver and Pharr method: (A) schematic curve of the nano-indentation test; (B) micrograph of the points load area; (C) nano-indentation load-displacement curves of 1 mN/s.

at the maximum load; *Er* is the reduced modulus; and E_i (1141 GPa) and v_i (0.07) are Young's modulus and Poisson's ratio of the diamond indenter, respectively [29]. Figure 11B shows the typical load-depth curves at 10,000 mN peak loads of the particles from the ITL to the HCCI matrix. About seven points give way to load the ITL (points 2–8), one point load particle (point 1), and matrix (point 9), respectively. Under the same peak load, the maximum penetration depth, final residual indentation depth, ITL, and matrix are different. In order to make the maximum penetration depth link with the final residual indentation depth, the relatively elastic recovery rate must be reviewed:

$$\delta = (h_m - h_{p'}) / h_m. \tag{11}$$

Figure 12 shows the results of relatively elastic recovery rate δ and recovery amount $h_{p'}$. The recovery amount of the ITL was better than those of the ceramics and the matrix. The δ of particles, ITL, and matrix was about 48.88%, 61.69%, and 51.32%, respectively. It can be concluded that the ITL exhibits good elastic and plastic property.

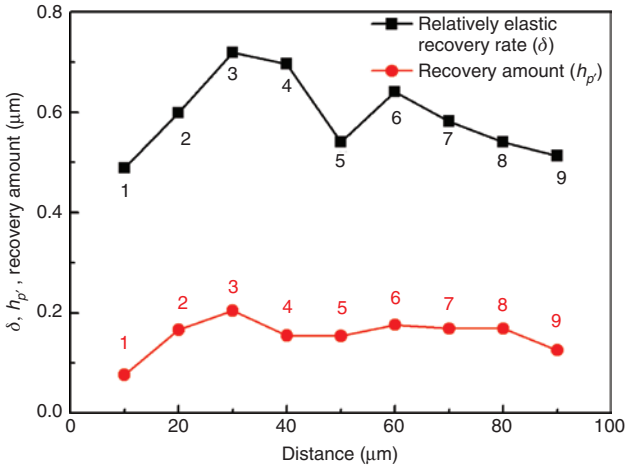

Figure 12: Results of relatively elastic recovery rate δ and recovery amount $h_{p'}$.

Figure 13A shows that the elastic modulus of the particles was larger than that of the HCCI matrix and ITL. Meanwhile, the elastic modulus of the HCCI matrix was larger than that of the ITL. It can therefore be concluded that the deformation capacity of the ITL under the same force is better than the particles and the HCCI matrix. It plays a very important role in bonding between the particles and the matrix; the particles and matrix possess different thermal expansion coefficients. Figure 13B contains information regarding the hardness of the composites. The hardness of the particles was higher than both the ITL and HCCI matrix. Thus, the ITL exhibits good mechanical properties. It also has good elasticity, which means it can absorb energy when the particles or the matrix thermally expand and contract. At the same time, it has a higher hardness, which means it has good wear resistance that prevents the particles from stripping.

3.3 Wear mechanism of composite

S_0, S_N, S_Y in Figure 14A and B represent the HCCI, without powder composites and with powder composites, respectively. Figure 14A shows the total volume loss of samples. The test results indicate that the wear resistance of the composites was seven times more than that of HCCI. Comparing the results of S_N and S_Y, the S_N wear resistance instability and the wear volume loss were larger.

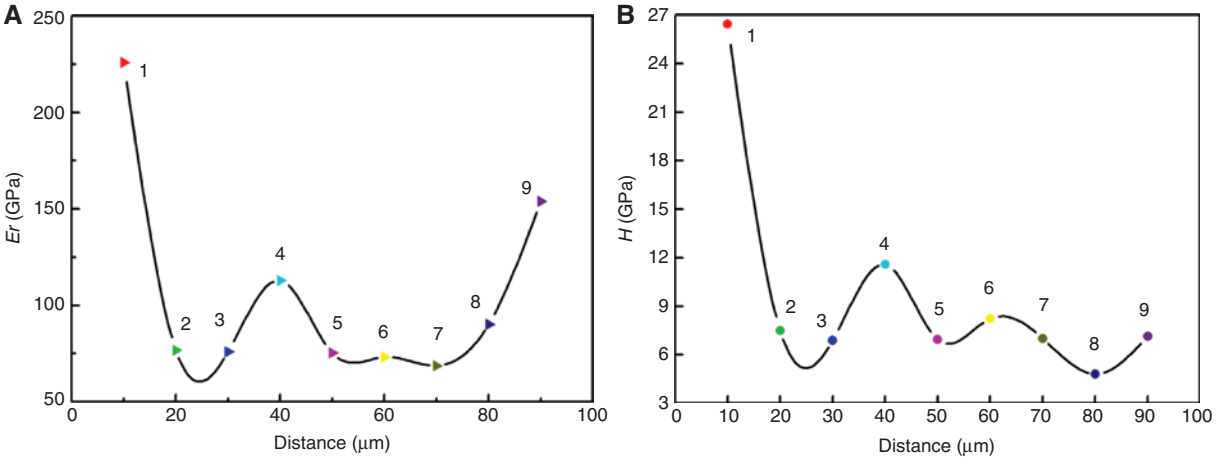

Figure 13: Results of (A) E_r and (B) hardness.

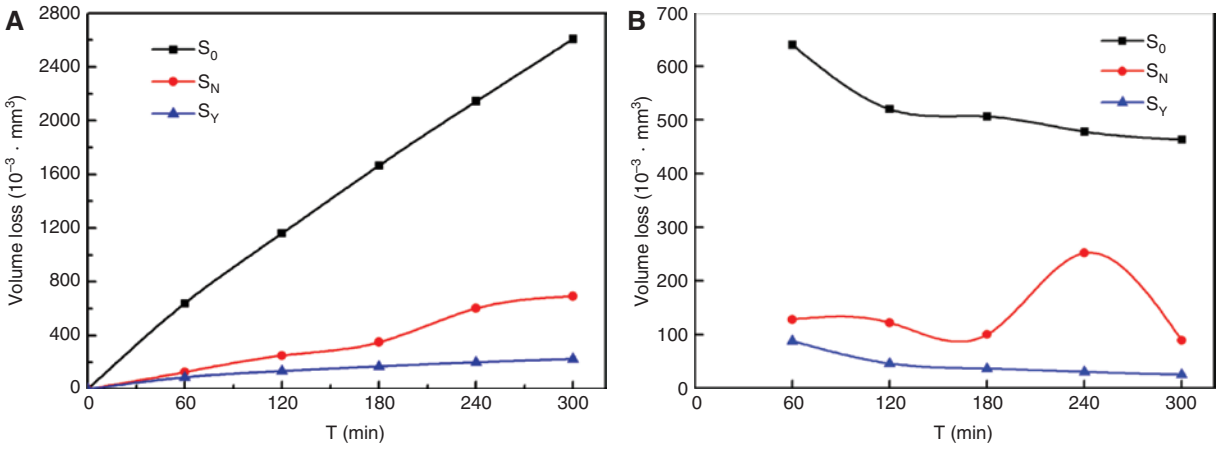

Figure 14: Wear results of samples: (A) total amount of volume loss; (B) volume loss in each test process.

Figure 14B shows the volume loss at each abrasive wear test process, and the results show that the S_N composites appear to have undergone significant fluctuations in the fourth process.

Figure 15 shows the scanning electron microscopy (SEM) micrographs of the abrasive wear area. Figure 15A indicates the experimental results of S_N, showing that the ceramic particles experienced shedding during the wear processes. Compared with sample S_Y (Figure 15B), S_N had a poor effect on the combined interface.

The three stages of wear mechanism are initial wear, wear interim, and later period (Figure 16). Before wear

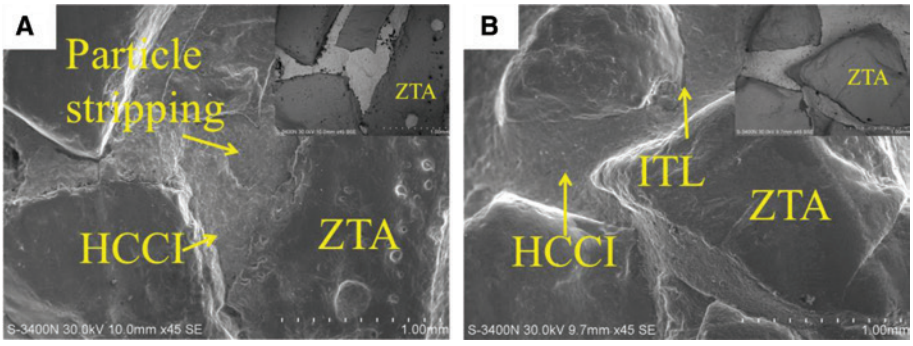

Figure 15: SEM micrographs of abrasive wear area: (A) samples of S_N; (B) samples of S_Y.

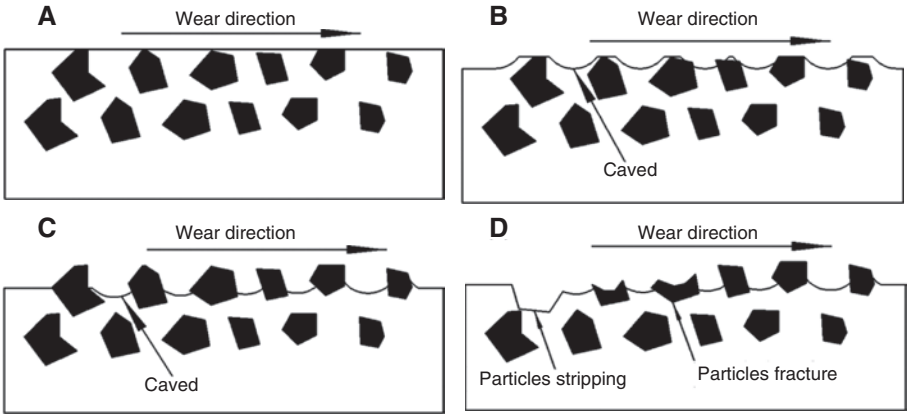

Figure 16: Schematic diagrams of the composite wear stages.

(Figure 16A), the particles were completely covered by the metal matrix that it can prevent the particles from stripping from the composites. With an increase in wear time, the initial wear period arrived (Figure 16B). The matrix between the particles created serious furrows by the abrasive particles because the abrasive hardness of quartz is higher than that of HCCI (HV600–800). The mass of composites was seriously reduced and formed caving between the ceramic particles [8]. As time continued, the interim wear stage arrived (Figure 16C). The ceramic particles stood out on the matrix and formed a "microcosmic shadow effect" to protect the matrix because of its high wear resistance. At the same time, the caved surface between the particles protected the particles, preventing them from fracture and stripping [30]. During the period (Figure 16D), the mass loss of the matrix was serious. The particles' massive exposure could not protect the matrix between the particles and the matrix could not support the particles simultaneously. Finally, the particles both fractured and stripped, and new particles then stood out and began the next cycle.

4 Conclusions

1. Ceramic particles reinforced HCCI matrix composites were successfully obtained, where the wear resistance of the composite was seven times higher than that of cast iron. The wear resistance of the composites with the transition layer was better than that without it.
2. HCCI and the transition layer completed metallurgical bonding through the diffusion and reaction of elements. The transition layer and the ceramic particles completed metallurgical bonding through the phases by merging together.

Acknowledgment: This work was supported by the National Natural Science Foundation of China (nos. 51571103, 51501079), the Yunnan Province Science Foundation for Youths (No. 2015FD009).

References

[1] Hutchings IM. *Mater. Sci. Eng. A Struct. Mater. Proper. Microstruct. Process.* 1994, 184, 185–195.
[2] Daniel BSS, Murthy VSR, Murty GS. *J. Mater. Process. Technol.* 1997, 68, 132–155.
[3] Schlenther E, Özcoban H, Jelitto H, Faller M, Schneider GA, Graule T, Aneziris CG, Kuebler J. *Mater. Sci. Eng. A* 2014, 590, 132–139.
[4] Ibrahim IA, Mohamed FA, Lavernia EJ. *J. Mater. Sci.* 1991, 26, 1137–1156.
[5] Selvakumar S, Dinaharan I, Palanivel R, Ganesh Babu B. *Mater. Sci. Eng. A* 2017, 685, 317–326.
[6] Prabhu TR, Varma VK, Vedantam S. *Wear* 2014, 309, 1–10.
[7] Konopka K, Olszówka-Myalska A, Szafran M. *Mater. Chem. Phys.* 2003, 81, 329–332.
[8] Zheng K, Gao Y, Tang S, Li Y, Ma S, Yi D, Zhang Z. *Tribol. Lett.* 2014, 54, 15–23.
[9] Zhang Z, Chen Y, Zhang Y, Gao K, Zuo L, Qi Y, Wei Y. *J. Alloys Comp.* 2017, 704, 260–268.
[10] Zhou R, Jiang Y, Lu D. *Wear* 2003, 255, 134–138.
[11] Li Z, Jiang Y, Zhou R, Lu D, Zhou R. *Wear* 2007, 262, 649–654.
[12] Zheng K, Gao Y, Li Y, Zhao S, Wang *J. Proc. Inst. Mech. Eng. J J. Eng. Tribol.* 2013, 228, 3–10.
[13] Ru J, Jia Y, Jiang Y, Feng J, Zhou R, Hua Y, Wang D. *Surf. Eng.* 2017, 33, 353–361.
[14] Leon CA, Drew RAL. *J. Mater. Sci.* 2000, 35, 4763–4768.
[15] Leon CA, Drew R. *Compos. A Appl. Sci. Manufact.* 2002, 33, 1429–1432.
[16] Exare C, Kiat J-M, Guiblin N, Porcher F, Petricek V. *J. Eur. Ceram. Soc.* 2015, 35, 1273–1283.
[17] Freim J, Mckittrick J. *J. Am. Ceram. Soc.* 2005, 81, 1773–1780.
[18] Chen J, Xie Z, Gui J, Wu W. *Ceram. Int.* 2016, 42, 17997–18003.
[19] Pulgarin HLC, Albano MP. *Ceram. Int.* 2014, 40, 5289–5298.
[20] Veit U, Rüssel C, Houet Y, Laurent D. *Ceram. Int.* 2015, 42, 5810–5822.
[21] Partyka J, Sitarz M, Leśniak M, Gasek K, Jeleń P. *Spectrochim. Acta A Mol. Biomol. Spectrosc.* 2015, 134, 621–630.
[22] Baasner A, Schmidt BC, Dupree R, Webb SL. *Geochim. Cosmochim. Acta* 2014, 132, 151–169.
[23] Induja IJ, Surendran KP, Varma MR, Sebastian M. *Ceram. Int.* 2017, 43, 736–740.
[24] Rosso M. *J. Mater. Process. Technol.* 2006, 175, 364–375.
[25] Xiao Z, Tan F, Wang W, Lu H, Cai Y, Qiu X, Chen J, Qiao X. *Ceram. Int.* 2015, 41, 325–331.
[26] Wang X. *Appl. Surf. Sci.* 2005, 252, 2021–2028.
[27] Sharma A, Lee BK. *Appl. Catal. A Gen.* 2016, 523, 272–282.
[28] Moosavi-Khoonsari E, Jung IH. *Metallurg. Mater. Trans. B* 2016, 37, 1–19.
[29] Donnelly E, Baker SP, Boskey AL, van der Meulen MCH. *J. Biomed. Mater. Res. A* 2006, 77, 426–435.
[30] Li Y, Gao Y. *Wear* 2010, 268, 511–518.